PROCEEDINGS OF SCIENCE

3D Models of Astrophysical Masers with Polarization

, M. D. Gray[a,*] K. Asanok[a] M. Phetra[b] T. Chanapote[a] and S. Etoka[c] B. Pimpanuwat[c]

[a] *National Astronomical Research Institute of Thailand, 260 Moo 4, T. Donkaew, A. Maerim, Chiang Mai 50180, Thailand*

[b] *Graduate School, Department of Physics & Material Science, Faculty of Science, Chaing Mai University, Chiang Mai 50200, Thailand*

[c] *Jodrell Bank Centre for Astrophysics, Department of Physics & Astronomy, University of Manchester M13 9PL, UK*

E-mail: malcolm@narit.or.th, kitiyanee@narit.or.th, mont21812@gmail.com, thanapol@narit.or.th, sandra.etoka@googlemail.com, bannawit.pimpanuwat@postgrad.manchester.ac.uk

Observational drivers for a Zeeman-based 3D maser radiation transfer code are discussed. We present basic information about the code and its methods of solving for molecular density-matrix elements. We consider tests of the model using a long cylindrical domain that offers hope of comparing the model with previous 1D results. Results are generated for cases of wide and narrow Zeeman splitting, as compared to the Doppler width. In the wide-splitting case, our model conforms with expectations for magnetic field orientations parallel and perpendicular to the long axis of the domain. Results in the narrow-splitting case are plausible, but need further work for confirmation. We demonstrate the ability to generate VLBI-style images as well as spectra averaged over a view of the domain.

15th European VLBI Network Mini-Symposium and Users' Meeting (EVN2022)
11-15 July 2022
University College Cork, Ireland

*Speaker

PoS(EVN2022)031

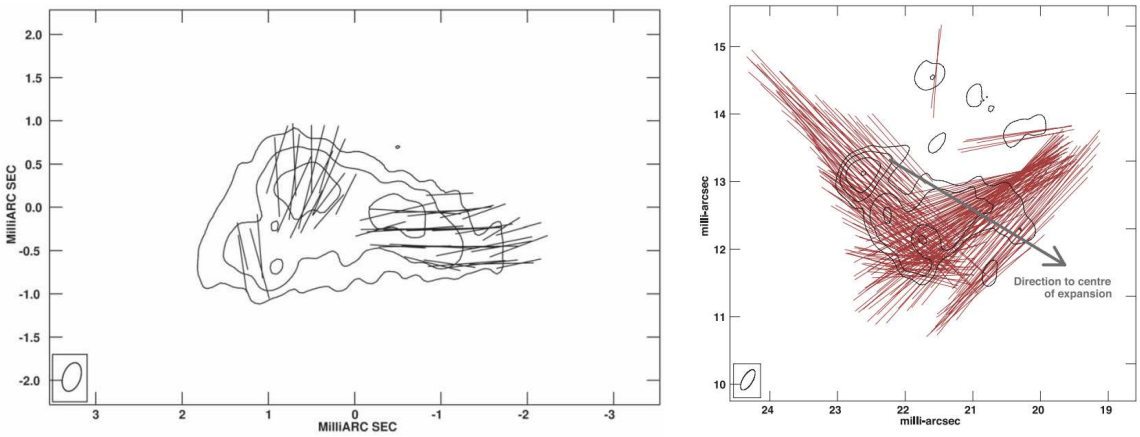

Figure 1: Examples of $\pi/2$ EVPA rotations within a single cloud at VLBI resolution: left, cloud with designation BD46AO in the South-West portion of the $v = 1, J = 1 - 0$ maser ring of TX Cam [5]; right, a cloud in the North-Eastern part of the maser ring of R Cas in the same transition [4].

1. Introduction

Silicon monoxide (SiO) masers in various rotational transitions from the first five vibrational states and several isotopologues are commonly observed towards the inner circumstellar envelopes of asymptotic giant branch (AGB) stars, particularly of the oxygen-rich, or M-type, class. These masers typically appear in the sky-plane as broken rings of emission, for example [1], that change in radius and flux density, following the light-curve of the host star, with a typical delay of 0.1-0.2 period with respect to the optical waveband. Maser rings have typical radii of a few stellar photospheric radii, and the radii vary with phase, cycle and rotational transition [2].

In a very small subset of stars, notably TX Cam and R Cas, full pulsation cycles have been followed at VLBI resolution and in full polarization. Towards the former star, linear polarization of 15-30% and 3-5% circular polarization were observed in the $v = 1, J = 1 - 0$ masers, and explained through a conventional Zeeman mechanism [1, 3]. A convective dynamo mechanism is suggested for providing magnetic fields of up to 500 G (0.05 T). Levels of polarization in R Cas are broadly consistent with those observed in TX Cam [4].

A phenomenon that is a driver for the model described in the present work is rotation of the EVPA (electric vector position angle) through approximately $\pi/2$, apparently within a single maser object or cloud that forms part of the incomplete ring described above. The EVPA is defined, to within a constant offset, as $(1/2)\arctan(U/Q)$, where U and Q are the Stokes parameters related to linear polarization. This type of EVPA rotation has been observed towards both TX Cam and R Cas, and examples are presented in Figure 1. The phenomenon covers a considerable range in polarized intensity, with the R Cas object peaking at 800 mJy(beam)$^{-1}$, compared with the TX Cam cloud at 10 mJy(beam)$^{-1}$.

2. Interpretation

The single-cloud EVPA rotation behaviour described in Section 1 has several possible interpretations. Importantly, the derived magnetic field strength may be wrong by more than an order of magnitude if an incorrect mechanism is assumed. We consider the Zeeman

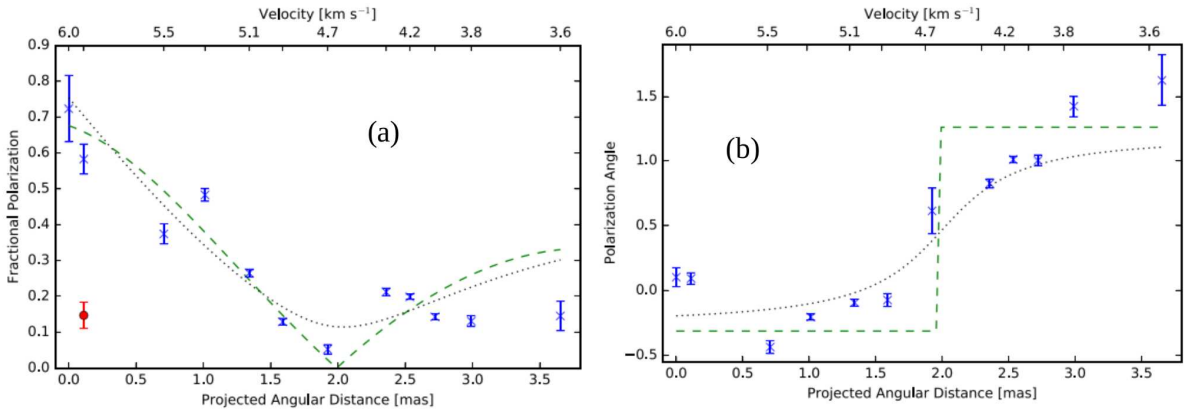

Figure 2: (a): The observed linearly polarized fraction of intensity, m_l, as a function of the angular distance across cloud BD46AO from TX Cam (blue symbols). The upper x-axis also shows this progression in Doppler velocity. (b): As for panel (a), but showing the variation of the EVPA across the same cloud. Both panels also show fits based on the analytical model from [6] with zero Stokes U (green lines) and a constant U/I (black dots). The red symbol marks a significant measurement of circular polarization.

interpretation and 3 others, investigated by [5], in more detail below. Reasonable magnetic field strengths in AGB circumstellar environments produce a Zeeman splitting ($g\Omega$) in SiO that is $\ll$ the thermal Doppler width ($\Delta\omega_D$). The saturation regime is moderate to strong, satisfying $g\Omega \gg R \gg \Gamma$ (the stimulated emission rate, R, greatly exceeds the loss rate, or homogeneous line width, Γ, while still being $\ll g\Omega$). In this regime, the magnetic field, **B**, provides a good quantization axis for the magnetic substates of the rotational states of SiO, and an EVPA switch is expected when the angle, θ, of **B** to the line of sight to the observer passes through the Van Vleck angle of $\simeq 54°.7$ [6]. In Figure 2, we show the linearly polarized fraction, $m_l = \sqrt{Q^2 + U^2}/I$, (a), left panel, and the EVPA (b), right panel as a function of angular distance across the cloud BD46AO from TX Cam, the object also shown in Figure 1 (left). These plots also show fit lines, based on models in [6], both with zero Stokes U, and with a constant U/I for θ satisfying $\sin^2\theta \geq 1/3$. The fits for m_l are broadly satisfactory, but the EVPA behaviour is considerably smoother than the model fit with $U/I = 0$, and does not have the restricted flip range of the model with constant U/I.

2.1 Local Magnetic Field Curvature

Suppose the π-type transition, dominates emission in the $J = 1 - 0$ Zeeman group: the electric dipole of this transition aligns with **B** under the splitting regime disussed above. If **B** lies close to the plane of the sky, the electric vector would then align with both dipole and **B**. If the sky-plane orientation of **B** varies across a cloud, we would then expect the EVPA to follow the field structure. The match of this model to the data has rather opposite behaviour to that of the Zeeman effect: the EVPA rotation could be arbitrarily smooth in order to match the data in Figure 2, panel (b), but the Van Vleck angle would have no special significance, and it is difficult to explain the pattern of obsevational points in Figure 2, panel (a).

2.2 Anisotropic Radiative Pumping

Linear polarization of SiO masers has been explained in terms of the Hanlé effect [7], where the electric field vector of the linearly polarized radiation is described by an anisotropy factor that can predict an EVPA flip from a tangential to a radial orientation with respect to the maser ring. While this stellar radiation-driven mechanism has not been ruled out, its effects are expected to decrease with radial distance from the photosphere. However, [1] observed increasing fractional linear polarization with radius in TX Cam.

2.3 Anisotropic Resonant Scattering

This mechanism converts Stokes Q and U to Stokes V via an interaction of the polarized radiation with magnetised foreground material [8]. Typical low fractions of circular polarization found in VLBI observations of AGB stars, of order $\leq$10%, require the foreground $\mathbf{B}$ almost $\perp$ to the electric field of the linearly polarized maser radiation. It seems unlikely that there are no cases where the field orientation is different, leading to circularly polarized fractions similar to those of the linearly polarized input maser radiation [5].

3. The New Model

The new 3D code uses Fourier-transformd equations to represent the molecular density matrix (DM) in the manner of [9]. Radiative transfer solutions, at the electric field level, are then used to analytically eliminate radiation quantities, leaving a set of non-linear algebraic equations in the elements of the DM that can be solved via methods similar to those in [10].

The goal for the code is to be able to analyse magnetic field changes in irregular objects of AU-scale, such as those seen in VLBI experiments. It is difficult to use the Stokes parameters in calculating solutions for the DM, since the solutions must consider rays arriving from all points on an external sphere, at a particular node of the model. Since the Stokes parameters are receiver-based, each ray would need its own private Stokes system. Therefore, we use instead simply the electric field components of each ray. It is also impractical to derive equations solely in the populations, or diagonal elements of the DM. We therefore solve directly for off-diagonal elements of the DM, from which populations or inversions can later be derived.

A further difficulty regarding testing the code is that there are only 1D models for comparison. Therefore, tube domains were constructed with a variety of axis ratios, with the thinner versions hopefully close enough to the 1D case, in terms of dominant rays along the long axis, for a meaningful comparison. An example domain, with a length-to-radius ratio of 10, is shown in Figure 3, panel (a). In panel (b) we show an example ray interacting with the DM at a particular node of the domain, where the magnetic field defines its own z-axis that is different from the global z-axis aligned with the long axis of the tube domain. Population solutions result from the saturation of the DM by the average electric field of many rays of this type, arriving from different directions. Once population solutions have been obtained, computionally cheap formal solutions (see Figure 3, panel (c)) allow an observer to view the domain from a large distance, and chosen direction, in terms of the

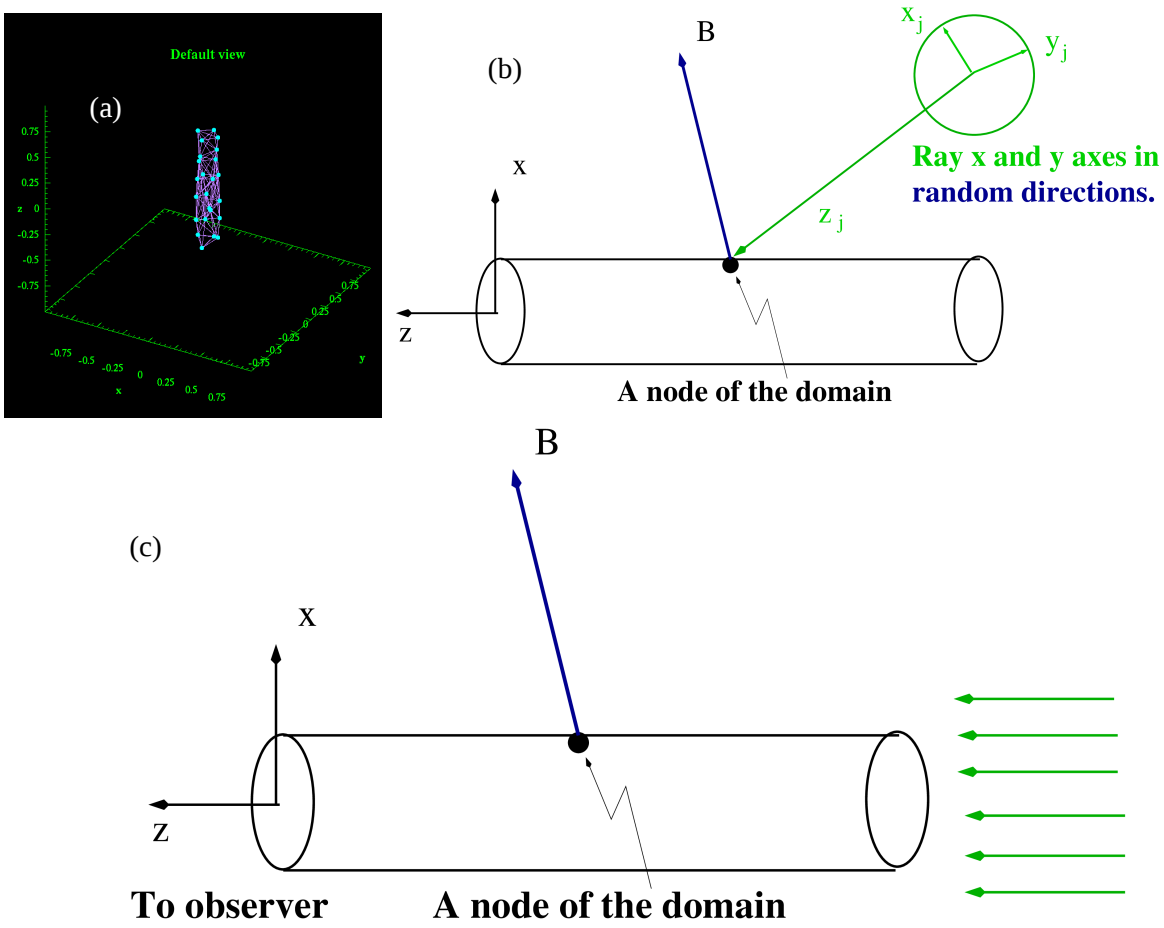

Figure 3: Panel (a): A view of the tube domain of length to radius ratio 10, with long axis aligned along the z-axis. Panel(b): A cartoon of the domain with a sample ray arriving at a particular domain node with a magnetic field close to the xy plane; this is the situtation for computation of a population (inversion) solution. Panel(c): A cartoon of a formal solution through the domain towards a distant observer placed on the z axis.

Stokes parameters derived from the electric fields of a set of nearly parallel rays. These formal solutions can be rendered as images, or avaraged over the projected domain as spectra.

4. Results of Tests

We adopt the following general conventions: a molecule with a Landé factor of the same sign as that of OH has the σ^+ transition as the lowest frequency in the Zeeman group; we adopt the IAU definition of Stokes V, that is the right-hand circular - left-hand circular polarized intensity. We use the IEEE axis system for formal solutions, in which the x-axis points North, and the y-axis, East as radiation approaches the observer.

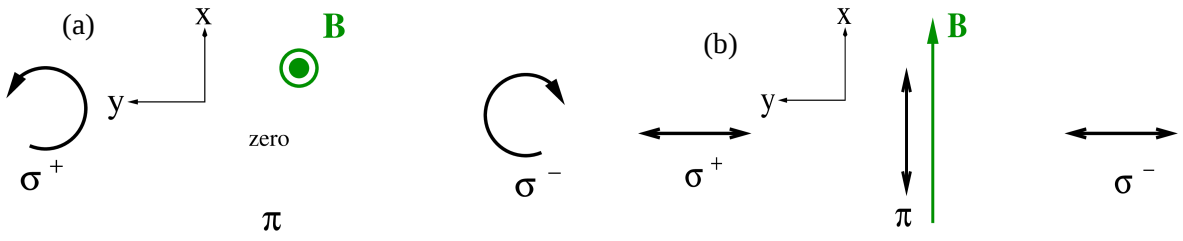

Figure 4: Polarization expectations for wide Zeeman splitting: (a) The magnetic field is aligned with the domain z-axis and points towards the observer; the π transition is absent, and the pair of σ transitions show opposite hands of circular polarization. (b) the magnetic field is aligned with the domain x-axis. The π dipole is aligned with the field, leading to positive Stokes Q. The σ dipoles, seen edge-on generate radiation with negative Q.

4.1 Wide-Splitting Tests

Two orientations of the magnetic field are considered for this case where $g\Omega \gg \Delta\omega_D$: one has $\mathbf{B} = B\hat{\mathbf{z}}$, and the other, $\mathbf{B} = B\hat{\mathbf{x}}$. Details regarding expected behaviour are shown in Figure 4. Output spectra, averaged over all the rays in each formal solution, are shown in Figure 5 for the two field orientations from Figure 4. In the case of the z-aligned field, panel (a), we see no evidence of a π-transition, as expected, because the dipole of this transition has no component $\perp$ to the propagation direction. The σ transitions appear with high levels of Stokes V and opposite hands of polarization. This is because the circular σ dipoles of opposite hands are presented face-on to the observer, and no direction in the xy plane is favoured for linear polarization.

When the magnetic field is x-aligned (Figure 5, panel (b)), we see that all significant polarization is linear as expected, with Stokes Q positive for the π-transition and negative for the σ transitions. The π dipole aligns with $\mathbf{B}$ (and therefore the x axis) leading to an x aligned electric field. In our convention Stokes Q is $I_x - I_y$, and is therefore positive. The σ dipoles appear edge-on to the observer, and both aligned with the y axis, leading to negative Q. Further tests were carried out for the magnetic field in the xy plane with both a y-aligned field and an intermediate angle to check that there is nothing special about aligning $\mathbf{B}$ with the x-axis.

4.2 Narrow-Splitting Tests

This case is typical of closed-shell molecules, such as SiO, H_2O and CH_3OH, where the Zeeman splitting is proportional to the nuclear magneton. We base our model on the $v = 1, J = 1 - 0$ transition of SiO with a rest frequency of 43.122 GHz and a splitting factor of $740.48\,\mathrm{s}^{-1}\,\mathrm{G}^{-1}$ [11], and we apply a magnetic field of B=10 G, so that each σ transition is shifted away from the pattern centre by $(1/2)g\Omega = 7404.8\,\mathrm{s}^{-1}$. Although this is rather a large field, it means that the Zeeman regime in Section 2 remains valid to a relatively high stimulated emission rate. In the models we discuss below the frequency channel width is equal to the Zeeman shift, and 30 channels cover 1.5 Doppler widths. As in Section 4.1, the long axis of the domain is z-aligned.

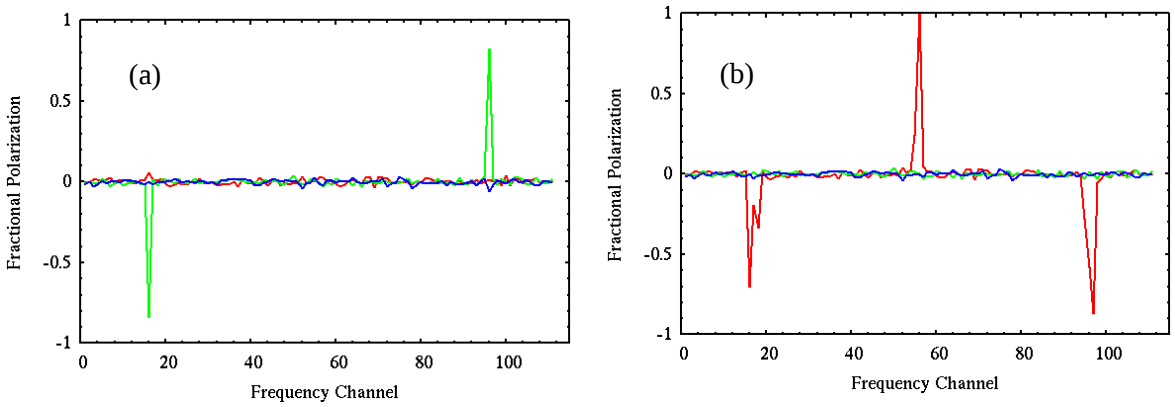

Figure 5: Fractional polarization in flux density shown as Q/I (red), U/I (blue) and V/I (green). Field orientations are (a) parallel to the domain z-axis and (b) parallel to the domain x-axis.

We computed DM solutions where the magnetic field has angles, θ, to the z-axis between 0 and 90°, and then used these in formal solutions for rays travelling in the positive z direction towards a distant observer. Background complex amplitudes of the electric field had independent x and y components each with a random phase uniformly distributed in the range $0..2\pi$, and a normally distributed real amplitude with a mean of $1/1000$ of the saturation value. We show sample fractional polarization spectra for $\theta = 0$ and 70° in Figure 6, noting that these are of duration equal to 1/(channel width in Hz). A smoothed spectrum, corresponding to the typical integration time of a single-dish radio telescope, would correspond to an average of several hundred to several thousand realisations, each based on different random complex amplitudes in the background. The spectra are at a maser depth (scaled distance) of 70.0, corresponding to considerable saturation: inversions in all three transitions in the most saturated nodes are typically 10-20% of the unsaturated value.

One useful test of the results is to plot the fractional linear polarization, m_l, see Section 2, as a function of θ, the angle between the magnetic field and the z axis. This plot should show a value of m_l close to zero at $\theta = 0$, and another minimum at the Van Vleck angle. Our plot for this model is shown in Figure 7. Error bars are estimated from the assumption that the fractional standard error in the Stokes parameters of highly amplified spectral channels is the same as in the background (0.125), and then following a standard error propagation for the uncertainty on m_l. The error bars should be considered a minimum estimate of the error, since there are also uncertainties in the DM solutions used in the formal solutions. The results in Figure 7 can be compared to the 1D model solutions in [12], specifically their Fig.10, and earlier work cited within, for example [13], Fig.1. Given these uncertainties, our results demonstrate at least qualitative agreement with earlier work.

It is also possible to show the brightness distribution in an image, simulating what would be observed by an interferometric observation of the domain. We show three examples in Figure 8 from the 70° model used above: Stokes I (left and right panels) and Stokes Q (middle panel). The colour bar to the right of each figure shows intensity as a multiple of the

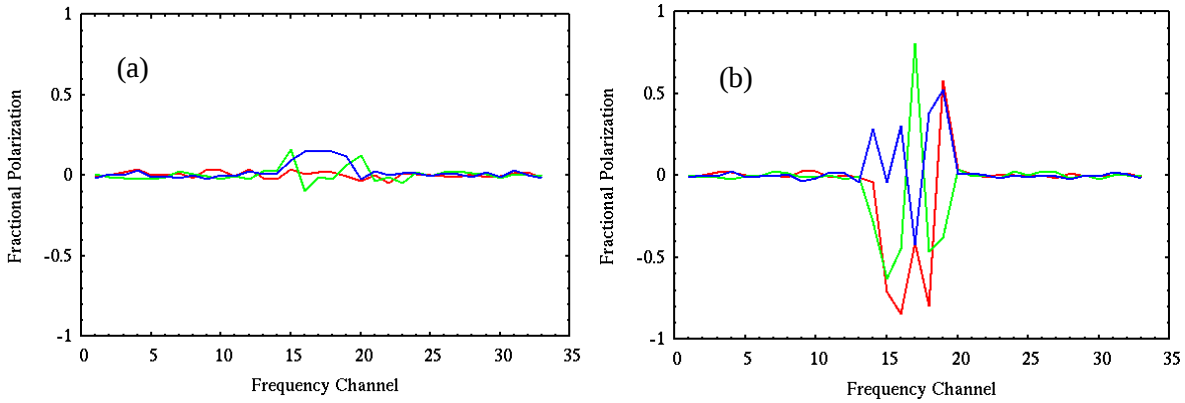

Figure 6: Fractional polarization in flux density shown as Q/I (red), U/I (blue) and V/I (green). Field orientations are (a) parallel to the domain z-axis and (b) at 70° to the z-axis. The magnetic field projection on the xy plane is parallel to the x axis.

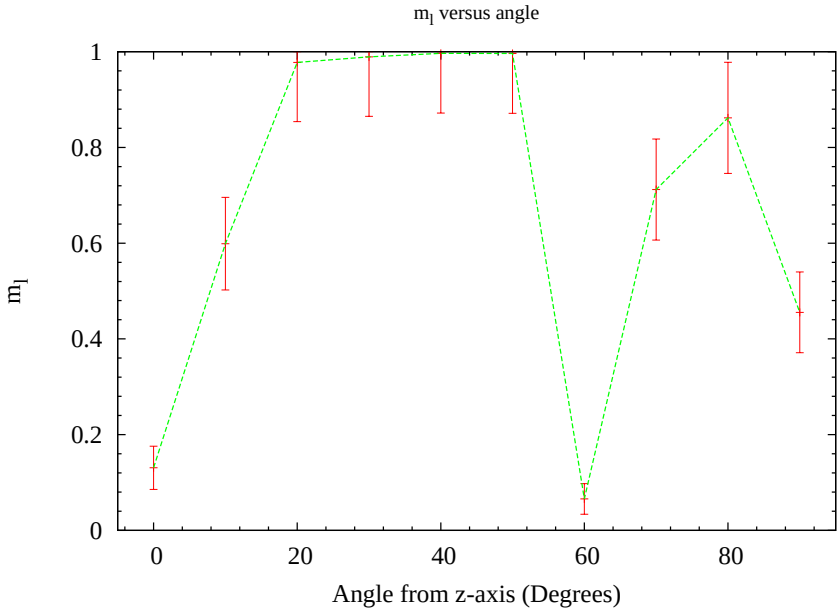

Figure 7: Fractional linear polarization m_l, as a function of the angle of the magnetic field from the domain z axis, at a maser depth of 70.0, corresponding to substantial saturation. The spectral channel used is 15.

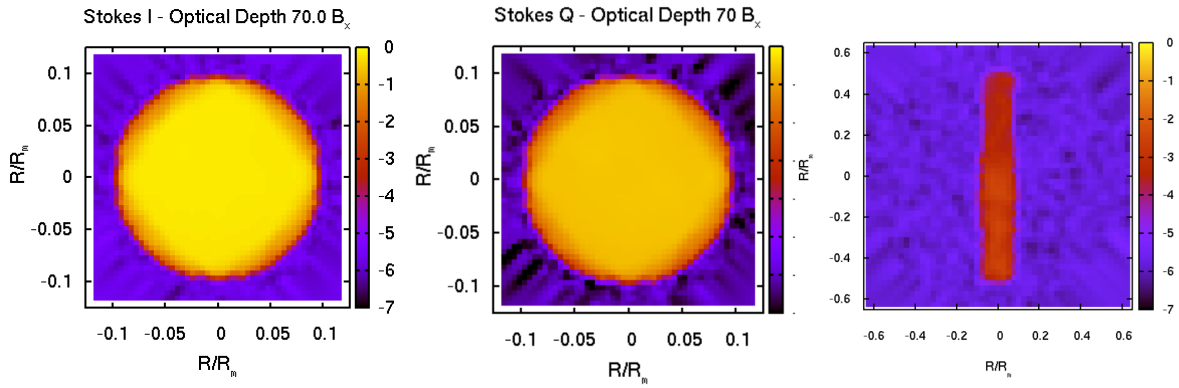

Figure 8: Synthetic images of the domain as seen by a distant observer on the z axis in Stokes I (left panel) and Stokes Q (middle panel). The third panel shows the domain in Stokes I, but for an observer on the x axis. Intensities are represented on a colour scale as multiples of the saturation intensity of the maser. There are 2352 rays, and the mean of the background level for Stokes I is 10^{-6}.

saturation intensity, I_s. The right-panel is a view of the domain along the x axis, also under strongly saturating conditions. Despite the saturation, short path lengths perpendcular to the domain axis limit intensities in this direction to $\sim 10^{-3}$ of I_s. As the domain is a tube, its full length of 1.0 domain units is visible in the right-hand panel. By contrast, the end views (left and centre panels) show the more compact end-on view of the tube, with a radius of 0.1 domain units. Rays passing along the length of the tube achieve intensities comparable to I_s. The distributions of intensity across the end-face of the domain appear quite smooth, and fall abruptly to the background level near the tube radius, almost certainly because the domain nodes are concentrated on the surface of the tube. As the background is unpolarized, its level for Stokes Q is much lower than for Stokes I. As a logarithmic intensity scale is used, the log of the magnitude of Stokes Q is plotted.

5. Conclusion

We have constructed a 3D maser polarization code in the hope of better understanding phenomena such as single-cloud scale EVPA rotations observed in circumstellar SiO masers. The model is Zeeman-based, but alternative polarization generation has not been excluded. The model has been tested in the wide and narrow Zeeman splitting regimes (relative to $\Delta\omega_D$). In the wide-splitting case, the model follows the expected polarization outcomes at large saturation. In the narrow splitting case, it is less clear that the model agrees with expectations, but linear polarization qualitatively follows the predictions of 1D models. Problems that remain to be addressed are the construction of solutions averaged over many realisations, and the analysis of circular polarization. Synthetic images of irregularly-shaped objects can be constructed in the Stokes parameters to simulate maps at VLBI resolution.

References

[1] A. J. Kemball, P. J. Diamond, I. Gonidakis, M. Mitra, K. Yim, K.-C. Pan, and H.-F. Chiang, *Multi-Epoch Imaging Polarimetry of the SiO Masers in the Extended Atmosphere of the Mira Variable TX Cam*, **698** (June, 2009) 1721–1739, [arXiv:0904.2621].

[2] I. Gonidakis, P. J. Diamond, and A. J. Kemball, *A long-term VLBA monitoring campaign of the v = 1, J = 1 0 SiO masers towards TX Cam - I. Morphology and shock waves*, **433** (Aug., 2013) 3133–3151, [arXiv:1306.0274].

[3] I. Gonidakis, P. J. Diamond, and A. J. Kemball, *Kinematics of the v=1, J=1-0 SiO masers at 43 GHz towards TX Cam - a new 73-frame movie*, **406** (July, 2010) 395–408.

[4] K. A. Assaf, P. J. Diamond, A. M. S. Richards, and M. D. Gray, *Polarization morphology of SiO masers in the circumstellar envelope of the asymptotic giant branch star R Cassiopeiae*, **431** (May, 2013) 1077–1089, [arXiv:1302.2530].

[5] T. L. Tobin, A. J. Kemball, and M. D. Gray, *Constraining Theories of Polarized SiO Maser Transport: Multi-epoch Analysis of a $\pi/2$ Electric Vector Rotation Feature*, **871** (Feb., 2019) 189.

[6] P. Goldreich, D. A. Keeley, and J. Y. Kwan, *Astrophysical Masers. 11. Polarization Properties*, **179** (Jan., 1973) 111–134.

[7] A. Asensio Ramos, E. Landi Degl'Innocenti, and J. Trujillo Bueno, *Dichroic Masers Due to Radiation Anisotropy and the Influence of the Hanle Effect on the Circumstellar SiO Polarization*, **625** (June, 2005) 985–995, [astro-ph/].

[8] M. Houde, *Non-Zeeman Circular Polarization of Molecular Maser Spectral Lines*, **795** (Nov., 2014) 27, [arXiv:1409.1594].

[9] L. N. Menegozzi and W. E. Lamb, Jr., *Laser amplification of incoherent radiation*, **17** (Feb., 1978) 701–732.

[10] M. D. Gray, J. Baggott, J. Westlake, and S. Etoka, *Maser flare simulations from oblate and prolate clouds*, **486** (Jul, 2019) 4216–4225, [arXiv:1904.1034].

[11] A. F. Pérez-Sánchez and W. H. T. Vlemmings, *Linear polarization of submillimetre masers. Tracing magnetic fields with ALMA*, **551** (Mar., 2013) A15, [arXiv:1301.0813].

[12] T. L. Tobin, M. D. Gray, and A. J. Kemball, *Polarized Maser Emission with In-Source Faraday Rotation*, *arXiv e-prints* (Dec., 2022) arXiv:2212.01410, [arXiv:2212.0141].

[13] W. D. Watson and H. W. Wyld, *The Relationship between the Circular Polarization and the Magnetic Field for Astrophysical Masers with Weak Zeeman Splitting*, **558** (Sept., 2001) L55–L58, [astro-ph/].

PoS(EVN2022)031